Measured g factors and the tidal-wave description of transitional nuclei near $A = 100$

S. K. Chamoli,[1] A. E. Stuchbery,[1] S. Frauendorf,[2] J. Sun,[2] Y. Gu,[2] R. F. Leslie,[1] P. T. Moore,[1] A. Wakhle,[1] M. C. East,[1] T. Kibédi,[1] and A. N. Wilson[1]

[1]*Department of Nuclear Physics, Research School of Physics and Engineering, Australian National University, Canberra, ACT 0200, Australia*

[2]*Department of Physics, University of Notre Dame, Notre Dame, Indiana 46556, USA*

(Received 17 February 2011; revised manuscript received 22 March 2011; published 20 May 2011)

The transient-field technique has been used in both conventional kinematics and inverse kinematics to measure the g factors of the 2_1^+ states in the stable even isotopes of Ru, Pd, and Cd. The statistical precision of the $g(2_1^+)$ values has been significantly improved, allowing a critical comparison with the tidal-wave version of the cranking model recently proposed for transitional nuclei in this region.

DOI: 10.1103/PhysRevC.83.054318 PACS number(s): 21.10.Ky, 27.60.+j, 25.70.De, 23.20.En

I. INTRODUCTION

The stable isotopes of $_{42}$Mo, $_{44}$Ru, $_{46}$Pd, and $_{48}$Cd include some of the best examples of vibrational level structures, with $^{110-116}$Cd, in particular, frequently being cited as "textbook" examples [1,2]. Recent studies indicate that the vibrational picture is reasonably good at the two-phonon level in $^{110-114}$Cd, but breaks down at the three-phonon level, particularly for non-yrast states [3].

The lower-mass stable isotopes and neutron-deficient isotopes of these elements are near $^{90}_{40}Zr_{50}$, which is almost double magic, and $^{100}_{50}Sn_{50}$, which is double magic. Having few valence nucleons, the level schemes therefore show spherical structures and are accessible to shell-model calculations [4]. By way of contrast with the spherical and vibrational structures in the low- and intermediate-mass isotopes, the heavier isotopes, with neutron numbers near midshell, make a transition to rotational structures. There has been considerable effort in recent years to study the spectroscopy of isotopes in this region produced either as fission fragments or as radioactive beams. Examples of experimental work relevant to this study are measurements of quadrupole moments and $B(E2)$ values in neutron-deficient Cd isotopes produced as radioactive beams [5], and measurements of g factors in neutron-rich fission fragments, in which a reduced magnitude for several neutron-rich nuclei was attributed to contributions from neutrons in the $h_{11/2}$ orbit [6,7].

On the experimental side, this paper focuses on measurements of the g factors of the first excited states in all of the stable even isotopes of Ru, Pd, and Cd by the transient-field technique. The precision is improved considerably compared with previous work.

On the theoretical side, we use the tidal-wave approach for calculating the g factors in this transitional region. The model uses the fact that, in the semiclassical approximation, the yrast states of vibrational nuclei correspond to quadrupole waves traveling over the surface of the nucleus like the tidal waves over the surface of the ocean. It has been demonstrated that the energies of the yrast states, as well as the $B(E2)$ values of the transitions between them, are very well described by this model for the even-even nuclei with $44 \leqslant Z \leqslant 48$ and $54 \leqslant N \leqslant 68$ [8,9]. This paper extends the model to g factors, which allows an examination of the way in which the angular momentum is shared between the protons and neutrons.

The paper is arranged as follows: Section II reports the g-factor experiments. The measurements using conventional kinematics are described first (Sec. II A), followed by the measurements using inverse kinematics (Sec. II B). A summary and discussion of adopted experimental g factors in Sec. II C completes the experimental part of the paper. The tidal-wave model calculations of the g factors are presented in Sec. III and the comparison between theory and experiment is discussed in Sec. IV. The conclusion follows (Sec. V).

II. TRANSIENT-FIELD g-FACTOR MEASUREMENTS

The g factors of the first excited states were measured in all the stable even isotopes of Ru, Pd, and Cd using the transient-field technique and beams from the Australian National University 14UD Pelletron accelerator. Measurements on the Cd and Ru isotopes in "conventional kinematics" are described in Sec. II A; those on the Ru, Pd, and Cd isotopes in "inverse kinematics" are described in Sec. II B. The experiments used the ANU Hyperfine Spectrometer [10]. Experimental procedures were similar to those described elsewhere [11–17].

Before describing the experiments, we review some procedures and terminology associated with the determination of the experimental g factors from transient-field precession measurements [11,13,14,18].

The observed transient-field precession $\Delta\Theta_{\rm obs}$ is related to the nuclear g factor g by

$$\Delta\Theta_{\rm obs} = g\phi(\tau), \tag{1}$$

where

$$\phi(\tau) = -\frac{\mu_N}{\hbar}\int_{t_i}^{t_e} B_{\rm TF}(v(t), Z)e^{-t/\tau}dt, \tag{2}$$

and μ_N is the nuclear magneton; τ is the mean life of the nuclear state, t_i and t_e are the times at which the ions enter into, and exit from, the ferromagnetic foil. The transient field strength $B_{\rm TF}(v(t), Z)$ depends on the atomic number and velocity of the ion within the ferromagnetic layer of the target.

It is often parametrized in the form

$$B_{\rm TF}(v, Z) = a_{\rm TF} Z^{p_Z} (v/v_0)^{p_v}. \quad (3)$$

For fully magnetized iron hosts, the Rutgers parametrization gives $a_{\rm TF} = 16.9$ T, $p_Z = 1.1$, and $p_v = 0.45$ [19].

As can be seen from Eq. (2), ϕ is a function of τ. In this paper, $\tau > 4$ ps while t_e is typically about 0.5 ps, so the exponential factor in Eq. (2) remains near unity; the observed precession is insensitive to τ, but not independent of it, especially for the shorter-lived states. Furthermore, for each isotope, the reaction kinematics, and slowing down of the ions in the ferromagnetic layer, are slightly different. It is useful to define the limiting case of ϕ for $\tau \to \infty$, namely,

$$\phi(\infty) = -\frac{\mu_N}{\hbar} \int_{t_i}^{t_e} B_{\rm TF}[v(t), Z] dt. \quad (4)$$

In the following presentation of experimental results, the observed precession angles $\Delta\Theta_{\rm obs}$ will always be given. Depending on what is known about the transient-field strength for the particular combination of ion and ferromagnetic host, it may be useful to present, in addition, a set of corrected experimental precessions for each isotope A, which reflect the relative g factors:

$$\Delta\Theta(A) = \Delta\Theta_{\rm obs}(A) \phi(\infty, A_{\rm ref})/\phi(\tau, A), \quad (5)$$

where $A_{\rm ref}$ denotes a chosen reference nuclide. The ratio of calculated ϕ values effectively removes the small differences in the measured precession angles due to differences in level lifetimes and reaction kinematics. In this paper, $\phi(\infty, A_{\rm ref})/\phi(\tau, A)$ is near unity. It is independent of the chosen transient-field scale parameter $a_{\rm TF}$, and is also insensitive to any reasonable choice of p_Z and p_v.

In some cases, it is appropriate to give experimental g factors relative to a reference g factor in the nucleus $A_{\rm ref}$, namely, $g_{\rm ref}(A_{\rm ref})$:

$$g(A) = g_{\rm ref}(A_{\rm ref}) \frac{\Delta\Theta_{\rm obs}(A)}{\Delta\Theta_{\rm obs}(A_{\rm ref})} \frac{\phi(\tau_{\rm ref}, A_{\rm ref})}{\phi(\tau, A)}, \quad (6)$$

where $\tau_{\rm ref}$ is the mean life of the reference state.

A. Conventional kinematics

1. Cd isotopes

The g factors of the first 2_1^+ states in ^{110,112,114,116}Cd were measured simultaneously, relative to each other, using the transient-field technique in conventional kinematics. The experiment was similar to that on the Mo isotopes [12]. Table I summarizes the relevant level properties and reaction kinematics.

States of interest were Coulomb excited using beams of 95 MeV ^{32}S. In the order encountered by the beam, the target consisted of layers of $^{\rm nat}$Ag, 0.05 mg/cm^2 thick, and $^{\rm nat}$Cd, 0.98 mg/cm^2 thick, which had been evaporated onto an annealed iron foil, 2.64 mg/cm^2 thick. On the back of the iron foil, a 5.47-mg/cm^2-thick layer of natural copper had already been evaporated. For additional mechanical support, and improved thermal contact with the cooled target mount, this multilayered target was pressed onto thicker ($\sim$12 μm) copper foil using an evaporated layer of indium as adhesive. Coulomb-excited Cd nuclei recoiled through the iron foil, where they experienced the transient field, and then stopped in the nonmagnetic copper layer where they subsequently decayed. The thin Ag layer on the front of the target was included to help protect the Cd layer, which has a low melting point of $\sim$321°C. To minimize the effect of beam heating on the target, it was maintained at a temperature of 6 K by mounting it on a cryocooler (Sumitomo RDK-408D). No deterioration of the Cd target layer was observed despite a high beam current of $\sim$12.5 pnA being maintained throughout the measurement ($\sim$4 days).

An external magnetic field of 0.09 T was applied perpendicular to the γ-ray detector plane to magnetize the ferromagnetic layer of the target. The direction of this field was reversed periodically to minimize systematic errors.

Backscattered beam ions were detected in a pair of silicon photodiode detectors, 10 mm high by 9 mm wide, placed 3.8 mm from the beam axis in the vertical plane parallel to the target, and 16 mm upstream of the target; the average scattering angle was 151°. To measure the transient-field precession, γ rays emitted in coincidence with backscattered particles

TABLE I. Level properties and reaction kinematics for Cd and Ru isotopes recoiling in iron after Coulomb excitation by 95-MeV ^{32}S beams. $E(2_1^+)$ is the energy and $\tau(2_1^+)$ is the mean life of the 2_1^+ level [20]. $\langle E_i \rangle$ and $\langle E_e \rangle$ are the average energies with which the ions enter into, and exit from, the iron foil. The corresponding ion velocities are $\langle v_i/v_0 \rangle$ and $\langle v_e/v_0 \rangle$. The average ion velocity is $\langle v/v_0 \rangle$. $v_0 = c/137$ is the Bohr velocity. $t_{\rm Fe}$ is the effective time for which the ions experience the transient field in the iron layer of the target. These quantities were calculated with the stopping powers of Ziegler *et al.* [21]. $\phi(\tau)$ is the transient-field precession per unit g factor calculated as described in the text.

Isotope	$E(2_1^+)$ (keV)	$\tau(2_1^+)$ (ps)	$\langle E_i \rangle$ (MeV)	$\langle E_e \rangle$ (MeV)	$\langle v_i/v_0 \rangle$	$\langle v_e/v_0 \rangle$	$\langle v/v_0 \rangle$	$t_{\rm Fe}$ (fs)	$\phi(\tau)$ (mrad)
^{110}Cd	657	7.4	51.6	8.4	4.35	1.75	2.77	543	−48.8
^{112}Cd	617	8.9	51.1	8.5	4.29	1.75	2.75	552	−49.4
^{114}Cd	559	13.7	50.7	8.6	4.23	1.75	2.72	564	−50.2
^{116}Cd	512	20.3	50.3	8.7	4.18	1.74	2.70	572	−50.8
^{100}Ru	540	18.2	58.6	12.3	4.86	2.23	3.34	410	−36.5
^{102}Ru	475	26.6	58.1	12.1	4.79	2.21	3.30	417	−36.2
^{104}Ru	358	83.4	57.6	12.5	4.72	2.20	3.26	426	−37.3

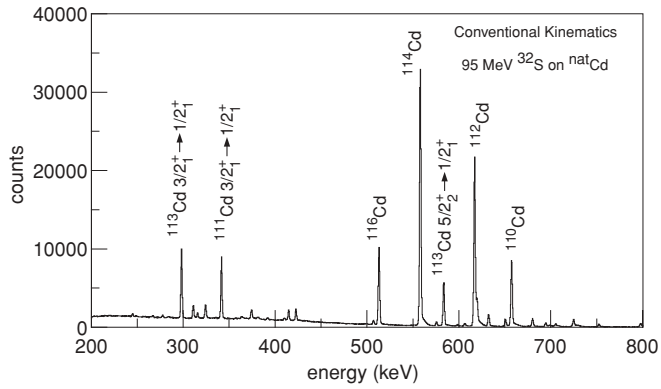

FIG. 1. Spectrum of γ rays observed at $+65^\circ$ to the beam axis in coincidence with backscattered ^{32}S beam ions. This spectrum represents all of the data for the field-up direction in the detector at $+65^\circ$, obtained during the precession measurement on the Cd target.

were observed in two 50% (relative efficiency) HPGe detectors and two 20% HPGe detectors placed at $\pm 65^\circ$ and $\pm 115^\circ$ to the beam axis, respectively. The target-detector distances were set so that the detector crystals all subtended a half angle of 18°. Figure 1 shows a coincidence γ-ray spectrum observed in the detector at $+65^\circ$ to the beam direction.

Particle-γ angular correlations were measured in a sequence of runs of about 75-min duration. The backward-placed Ge detectors were kept at $\pm 115^\circ$ to normalize the number of counts, while the angular correlation was sampled with the two forward Ge detectors at $\pm 25^\circ$, $\pm 35^\circ$, $\pm 45^\circ$, $\pm 55^\circ$, and $\pm 65^\circ$, in turn. The measured angular correlations for the $2^+_1 \rightarrow 0^+_1$ transitions are compared with the calculated angular correlations in Fig. 2.

The transient-field precession angles $\Delta\Theta$ were determined by the usual procedures [11,13,18,22]. Briefly, $\Delta\Theta = \epsilon/S$, where ϵ is the effect and $S(\theta_\gamma) = (1/W)dW/d\theta$, often referred to as the slope, is the logarithmic derivative of the angular correlation at the γ-ray detection angle θ_γ. Formally, $\epsilon = (N\downarrow - N\uparrow)/(N\downarrow + N\uparrow)$, where $N\uparrow$ ($\downarrow$) refers to the counts recorded for field up (down) at $+\theta_\gamma$; however, the evaluation of ϵ from the experimental data proceeds via the formation of a double ratio of counts recorded for field up and field down in a pair of detectors at $\pm\theta_\gamma$.

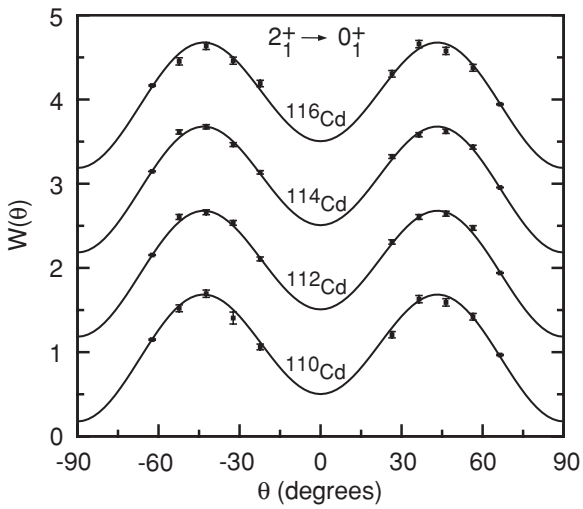

FIG. 2. Experimental and calculated angular correlations for even-A Cd isotopes following Coulomb excitation with 95-MeV ^{32}S beams. (Data for the different isotopes have been offset for presentation.)

Results of the precession measurements on the 2^+_1 states of the even Cd isotopes are given in Table II. Differences in the slopes $S(65^\circ)$ stem mainly from differences in the small level of feeding intensity from the higher excited states, especially the 4^+_1 state. The effect of this feeding contribution on the extracted g factors was evaluated as described in Ref. [15]. It was found that *extreme* values must be assumed for the magnitude of $g(4^+_1)$ in order to make even a few percent change in the precession observed for the 2^+_1 state. The effect of the feeding contribution is therefore accurately included in the present analysis by evaluating S for the fed (i.e., observed) angular correlation for the 2^+_1 state.

The absolute values of the g factors in the Cd isotopes were determined by reference to ^{106}Pd in the inverse kinematics measurements described below. Specifically, the precessions measured (in inverse kinematics) for ^{112}Cd and ^{114}Cd beams gave $g(^{112}\text{Cd}) = +0.365(30)$ and $g(^{114}\text{Cd}) = +0.313(25)$. Combining these values with the precessions for these isotopes in Table II determines that the absolute g factors in Table II are given by $g = \Delta\Theta/\phi(\infty) = \Delta\Theta/(-50.34 \pm 3.08)$, where $\Delta\Theta$ is in mrad.

A measurement on ^{110}Cd by Benczer-Koller *et al.* [23], in which the transient-field strength was determined by the Rutgers parametrization [19], gave $g(2^+_1;^{110}\text{Cd}) = +0.382(17)$, in very good agreement with the value obtained here. Our work therefore confirms the Rutgers parametrization of the transient-field strength for ions with $Z \sim 46 - 48$ traversing iron foils with velocities in the range $2v_0 \lesssim v \lesssim 4v_0$. For this reason, the values of $\phi(\tau)$ shown in Table I were evaluated using the Rutgers parametrization [19] in Eq. (2).

The g factors of several states in the two odd-A isotopes ^{111}Cd and ^{113}Cd were measured as a by-product of the measurement on the natural target. These results will be presented and discussed elsewhere [24].

2. *Ru isotopes*

The g factors of the first 2^+_1 states in ^{100,102,104}Ru were measured simultaneously, relative to each other, using the transient-field technique in conventional kinematics and procedures very similar to those described in Sec. II A1. States of interest were again Coulomb excited using beams of 95-MeV ^{32}S. The target consisted of a layer of ^{nat}Ru, 0.63 mg/cm^2 thick, which had been sputtered onto an annealed iron foil, 2.34 mg/cm^2 thick. The iron foil was then pressed onto a 12.5-μm-thick copper foil using an evaporated layer of indium, $\sim$3 mg/cm^2 thick, as adhesive. Coulomb-excited Ru nuclei recoiled through the iron foil, where they experienced the transient field, and then stopped in the nonmagnetic indium and copper layers, where they subsequently decayed. (Both indium and copper have cubic crystalline structure, so quadrupole interactions for the 2^+ states of the Ru isotopes are negligible in both host materials.)

TABLE II. Results of precession measurements and g factors for the 2_1^+ states in Cd isotopes (conventional kinematics). $|S(65^\circ)|$ is the logarithmic derivative of the angular correlation. $\Delta\Theta_F$ and $\Delta\Theta_B$ are the precession angles observed with the γ-ray detector pairs at $\pm 65^\circ$ and $\pm 115^\circ$, respectively; $\langle\Delta\Theta\rangle_{\rm obs}$ is the average of these. $\Delta\Theta$ has been corrected for small differences in the reaction kinematics as the ions traverse the iron layer of the target, so that relative values of $\Delta\Theta$ give relative g factors.

Isotope	$\lvert S(65^\circ)\rvert$ (rad^{-1})	$\Delta\Theta_F$ (mrad)	$\Delta\Theta_B$ (mrad)	$\langle\Delta\Theta\rangle_{\rm obs}$ (mrad)	$\Delta\Theta$ (mrad)	$g/g(^{116}\mathrm{Cd})$	g[a]
^{106,108}Cd[b]	2.8	−18(4)	−27(4)	−21.7(26)	−22.2(27)	1.51(20)	+0.44(6)
^{110}Cd	2.74	−19.9(9)	−19.7(12)	−19.79(74)	−20.32(76)	1.38(9)	+0.404(29)
^{112}Cd	2.71	−17.3(6)	−18.2(8)	−17.61(48)	−17.90(49)	1.22(7)	+0.356(24)
^{114}Cd	2.69	−15.9(5)	−16.6(6)	−16.18(39)	−16.18(39)	1.10(6)	+0.321(21)
^{116}Cd	2.70	−14.9(10)	−14.7(13)	−14.87(78)	−14.73(77)	1	+0.292(24)

[a]Assigned errors include the uncertainty in the transient-field calibration.
[b]Results for the composite 635-keV line, which includes both ^{106}Cd and ^{108}Cd, are included to show consistency with the measurements on these isotopes reported below.

Save for the different target, the experiment was essentially identical to that on the Cd isotopes reported in the previous section. The total beam time for the precession measurement was about 60 hours. Table I includes a summary of the relevant level properties and reaction kinematics. Figure 3 shows a coincidence γ-ray spectrum observed in the detector at $+65^\circ$ to the beam direction. Although natural Ru contains ^{96}Ru (5.5%), ^{98}Ru (1.9%), ^{99}Ru (12.7%), and ^{101}Ru (17.0%), along with ^{100}Ru (12.6%), ^{102}Ru (31.6%), and ^{104}Ru (18.7%), transient-field precessions could be obtained with meaningful precision only for the latter three isotopes.

Particle-γ angular correlations were measured in a sequence of runs of about 50-min duration. The two Ge detectors at negative angles were kept at -65° and -115° to normalize the number of counts, while the angular correlation was sampled at a sequence of angles in the positive hemisphere with the other two Ge detectors. The procedure was then reversed: the detectors at positive angles remained fixed, while the detectors at negative angles were moved to a sequence of angles. The measured angular correlations are compared with the calculated angular correlations in Fig. 4.

The absolute values of the g factors in the Ru isotopes as presented in Table III were determined by use of the Rutgers parametrization [19], which was demonstrated in the previous section (II A1) to be applicable for ions traversing iron hosts under the conditions of this measurement. The uncertainties shown in Table III correspond to the uncertainties in the relative g factors. Uncertainties on the absolute values of the g factors will be discussed in Sec. II C below, where these

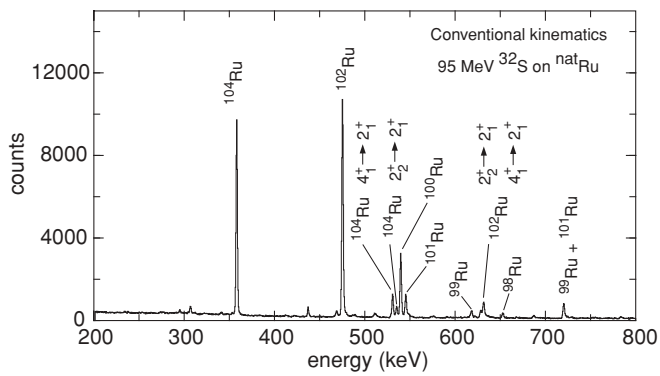

FIG. 3. Spectrum of γ rays observed at $+65^\circ$ to the beam axis in coincidence with backscattered ^{32}S beam ions. This spectrum represents the data for the field-up direction in the detector at $+65^\circ$, obtained during the precession measurement on the natural Ru target.

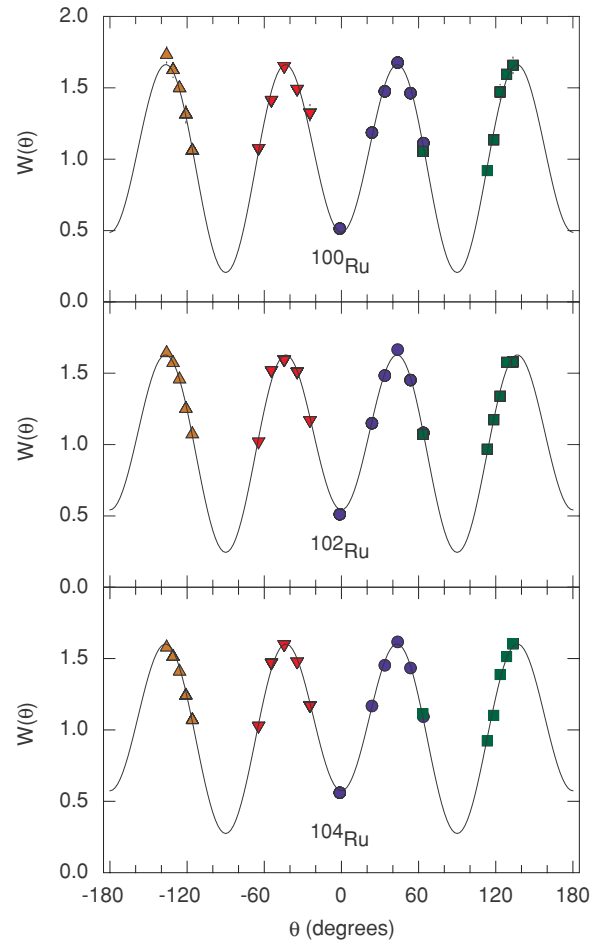

FIG. 4. (Color online) Experimental and calculated angular correlations for even-A Ru isotopes following Coulomb excitation with 95-MeV ^{32}S beams. Different symbols represent the four γ-ray detectors.

TABLE III. Results of precession measurements and g factors for the 2_1^+ states in Ru isotopes (conventional kinematics). The transient-field strength was calibrated using the Rutgers parametrization [19].

Isotope	$\lvert S(65^\circ)\rvert$ (rad^{-1})	$\langle\Delta\Theta\rangle$ (mrad)	$g/g(^{104}\mathrm{Ru})$	g[a]
^{100}Ru	2.72	−15.88(84)	1.08(7)	+0.434(23)
^{102}Ru	2.59	−16.85(44)	1.14(5)	+0.457(12)
^{104}Ru	2.50	−14.94(45)	1	+0.401(12)

[a]No uncertainty in the transient-field calibration is included here. Adopted g factors, including uncertainties in the field strength, are presented in Sec. II C.

measurements will be combined with the measurements in inverse kinematics.

B. Inverse kinematics: Ru, Pd, and Cd isotopes

As summarized in Table IV, transient-field measurements in inverse kinematics were performed on all of the stable even Ru and Pd isotopes, and ^{106,108,112,114}Cd, using ∼2.3-MeV/A beams from the 14UD Pelletron. The beam intensities ranged from ∼0.5 pnA for ^{106}Pd to ∼0.03 pnA for ^{98}Ru. Negative ion beams of the Ru and Pd isotopes were produced from natural metal powder pressed into a standard copper cathode. CdO^- beams were produced from cadmium oxide, natural for the ^{112}Cd and ^{114}Cd beams, and partially enriched for the ^{106}Cd and ^{108}Cd beams. Beams of $^{98}MoO_2^-$ ions were obtained from a metallic Mo cathode in the presence of O_2 gas.

For these inverse kinematics experiments, the ANU Hyperfine Spectrometer was configured with a forward array of three particle detectors; the apparatus and experimental procedures were similar to those in our recent work on the Fe isotopes [16,17].

The first two targets (labeled I and II) used for these measurements consisted of C layers on 6.1-mg/cm^2-thick copper-backed gadolinium foils. After rolling and annealing under vacuum, a thin 0.04-mg/cm^2 layer of copper was evaporated onto the beam-facing side (front) of the gadolinium foil to assist the adhesion of the C layer, and a thicker 5.5-mg/cm^2 layer of copper was evaporated on the back. The layer of carbon, 0.4 mg/cm^2 thick, was added to the front of the target by applying a suspension of carbon powder in isopropyl alcohol. Additional copper foil (4.5 mg/cm^2) was placed behind the target to stop the beam. The target was cooled below 5 K, both to minimize the effect of beam heating and to maximize the magnetization of the gadolinium layer of the target. Although they were nominally the same, Target I gave somewhat larger precessions for ^{108}Pd ions at 245 MeV than Target II. We attribute this difference to variations in the effective thickness of the target layers at the beam spot. It is also possible that the magnetization differs, despite the targets having been prepared from the same annealed gadolinium foil. An external magnetic field of 0.09 T was applied perpendicular to the γ-ray detection plane to magnetize the gadolinium layer of the target. This field was reversed periodically throughout the measurements.

TABLE IV. Summary of measurements in inverse kinematics. E_B and I_B are the beam energy and intensity.

Beam	E_B (MeV)	I_B (enA)	Measurement[a]; Purpose	Duration (h)
			Target I	
^{102}Ru^{16+}	245	5	ϵ; $g(^{102}\mathrm{Ru})/g(^{108}\mathrm{Pd})$	2.5
^{108}Pd^{15+}	230	5	ϵ; $B_{\mathrm{TF}}(v)$	2
^{108}Pd^{15+}	245	5	ϵ; $B_{\mathrm{TF}}(v)$	2.25
^{108}Pd^{17+}	260	5	ϵ; $B_{\mathrm{TF}}(v)$	1.75
^{114}Cd^{16+}	240	5	ϵ; $g(^{114}\mathrm{Cd})/g(^{108}\mathrm{Pd})$	5.5
			Target II	
^{96}Ru^{16+}	240	1.5	ϵ; $g(^{96}\mathrm{Ru})$	10
^{98}Ru^{16+}	240	0.5	ϵ; $g(^{98}\mathrm{Ru})$	25
^{100}Ru^{16+}	240	4	ϵ; $g(^{100}\mathrm{Ru})$	4.5
^{102}Ru^{16+}	240	3	ϵ; $g(^{102}\mathrm{Ru})$	1
^{104}Ru^{16+}	240	5	ϵ; $g(^{104}\mathrm{Ru})$	2
^{102}Pd^{16+}	245	0.8	ϵ; $g(^{102}\mathrm{Pd})$	8
^{104}Pd^{16+}	245	6	ϵ; $g(^{104}\mathrm{Pd})$	2.2
^{106}Pd^{16+}	245	8	ϵ; TF calibration	3.3
^{108}Pd^{16+}	245	6	ϵ,$W(\Theta)$; $g(^{108}\mathrm{Pd})$	3.5
^{110}Pd^{16+}	245	3	ϵ; $g(^{110}\mathrm{Pd})$	1.7
^{106}Cd^{16+}	240	2	ϵ; $g(^{106}\mathrm{Cd})$	9.6
^{108}Cd^{16+}	240	2	ϵ; $g(^{108}\mathrm{Cd})$	11
^{112}Cd^{16+}	240	1.4	ϵ; $g(^{106,108}\mathrm{Cd})/g(^{112}\mathrm{Cd})$	18
			Target III	
^{98}Mo^{16+}	240	2.2	ϵ; TF calibration	18
^{96}Ru^{16+}	240	2.5	ϵ; $g(^{96}\mathrm{Ru})$	18
^{100}Ru^{16+}	240	2.5	ϵ; $g(^{100}\mathrm{Ru})$	12
^{102}Ru^{16+}	240	2.5	ϵ; $g(^{102}\mathrm{Ru})$	15
^{104}Ru^{16+}	240	2.5	ϵ; $g(^{104}\mathrm{Ru})$	10
^{106}Pd^{16+}	240	2	ϵ; TF calibration	12

[a]ϵ: transient-field precession; $W(\Theta)$: angular correlation.

Additional experiments were performed with a third target (labeled Target III), which consisted of enriched ^{26}Mg, 0.45 mg/cm^2 thick, evaporated onto gadolinium, 3.2 mg/cm^2 thick, which was followed by layers of nickel (0.01 mg/cm^2) and copper (5.4 mg/cm^2). This target had previously been used for similar measurements at Yale by Taylor *et al.* [25].

Level properties of the beam ions and the reaction kinematics for target ions (^{12}C or ^{26}Mg) scattered into the outer particle detectors (average scattering angle 20.7°) are summarized in Table V.

The de-exciting γ rays from the Mo, Ru, Pd, and Cd isotopes were measured in coincidence with forward-scattered target ions detected by an array of three silicon photodiode detectors downstream from the target, arranged in a vertical stack as described in [16]. For the measurements in inverse kinematics, two 50% efficient HPGe detectors and two 12.7 cm by 12.7 cm NaI detectors were placed in pairs at ±65° and ±115° to the beam axis, respectively. The target-detector distances were again set such that the detector crystals all subtended a half angle of 18°. Figure 5 shows examples of coincidence γ-ray spectra observed in the Ge detector at +65° to the beam direction and the NaI detector at +115° to the beam.

Angular correlations were measured for ^{108}Pd beams at 245 MeV in a sequence of runs of about 20-min duration.

TABLE V. Level properties and reaction kinematics for Mo, Ru, Pd, and Cd beam ions recoiling in gadolinium after Coulomb excitation on target ions in inverse kinematics during the g-factor measurements. The reaction kinematics are shown for recoiling ^{12}C (Targets I and II) or ^{26}Mg (Target III) ions detected in the outer-particle counters (average scattering angle 20.7°). See Table I and text.

Isotope	E_B (MeV)	$E(2_1^+)$ (keV)	$\tau(2_1^+)$ (ps)	$\langle E_i\rangle$ (MeV)	$\langle E_e\rangle$ (MeV)	$\langle v_i/v_0\rangle$	$\langle v_e/v_0\rangle$	$\langle v/v_0\rangle$	t_{Gd} (fs)
				Targets I and II					
^{96}Ru	240	832.6	4.1	136.5	29.7	7.57	3.53	5.38	576
^{98}Ru		652.4	8.8	137.6	30.9	7.52	3.56	5.34	614
^{100}Ru		539.6	18.2	138.8	32.0	7.48	3.60	5.32	638
^{102}Ru		475.1	26.6	139.9	33.3	7.44	3.63	5.32	644
^{104}Ru		358.0	83.4	141.0	33.5	7.39	3.65	5.31	653
^{102}Pd	245	556.4	16.6	142.4	32.3	7.49	3.57	5.32	637
^{104}Pd		555.8	14.4	143.6	33.6	7.44	3.61	5.33	633
^{106}Pd		511.9	17.6	144.7	34.8	7.42	3.64	5.33	633
^{108}Pd		434.0	34.7	145.8	35.9	7.38	3.66	5.32	647
^{110}Pd		373.8	63.5	146.9	37.1	7.34	3.69	5.31	652
^{106}Cd	240	632.6	9.8	140.6	31.4	7.31	3.46	5.16	643
^{108}Cd		633.0	9.3	141.7	32.6	7.27	3.49	5.17	641
^{112}Cd		617.5	8.9	143.9	34.9	7.19	3.54	5.18	638
^{114}Cd		558.5	13.7	144.8	35.9	7.16	3.56	5.16	652
				Target III					
^{98}Mo	240	787.4	5.1	89.3	37.8	6.06	3.94	4.93	367
^{96}Ru		832.6	4.1	87.1	34.9	6.05	3.83	4.86	368
^{100}Ru		539.6	18.2	90.1	37.7	6.03	3.90	4.88	385
^{102}Ru		475.1	26.6	91.6	39.1	6.02	3.93	4.89	385
^{104}Ru		358.0	83.4	93.1	40.1	6.01	3.96	4.90	386
^{106}Pd		511.9	17.6	94.1	40.3	5.98	3.92	4.87	384

The backward-placed NaI detectors were kept at ±115° to normalize the number of counts, while the angular correlation was sampled with the two forward Ge detectors at ±30.5°, ±35°, ±45°, ±55°, and ±65°, in turn. The results of these measurements are compared with the calculated angular correlations in Fig. 6. Calculated angular correlations were used for the analysis of the precession data. At the relatively low beam energy of ∼ 2.3 MeV/nucleon, multiple excitation is very small and the angular correlations for all isotopes are effectively identical [17]. The slope parameters are $S(65°) = -2.69$ rad^{-1} for the outer particle counters and $S(65°) = -2.60$ rad^{-1} for the center detector.

The velocity dependence of Pd ions traversing gadolinium was investigated through measurements on 230, 245, and 260 MeV ^{108}Pd ions traversing Target I. The results are summarized in Table VI. In these measurements, the Pd ions sample the transient field over a velocity range that extends beyond that covered in the g-factor measurements. Between the three runs at different beam energies, there is an overlap of the velocity range sampled by the ^{108}Pd ions in consecutive measurements due to the difference in scattering conditions for the center-particle ($\langle\theta_{\mathrm{C}}\rangle = 0°$) and outer-particle ($\langle\theta_{\mathrm{O}}\rangle = 20.7°$) detectors. Agreement between the observed precessions for the measurements that span similar velocity ranges is excellent. Figure 7 compares the velocity dependence of the average transient-field strength for Pd ions traversing gadolinium with that of the Rutgers parametrization. While the field-strength parameter a_{TF} has to be scaled up by a factor of about 1.4 for Target I, the data are nevertheless consistent with a $v^{0.45}$ dependence over the range applicable for the present g-factor measurements. To evaluate relative g factors, we have therefore used the Rutgers

TABLE VI. Reaction kinematics, precessions, and average transient-field strengths for ^{108}Pd. See Tables I and II and text. $\langle\theta_{\mathrm{carbon}}\rangle$ is the average scattering angle of the carbon target ions.

E_B (MeV)	$\langle\theta_{\mathrm{carbon}}\rangle$ (degrees)	$\langle E_i\rangle$ (MeV)	$\langle E_e\rangle$ (MeV)	$\langle v_i/v_0\rangle$	$\langle v_e/v_0\rangle$	$\langle v/v_0\rangle$	t_{Gd} (fs)	$\Delta\Theta_{\mathrm{obs}}$ (mrad)	$\langle B_{\mathrm{TF}}\rangle$ (ktesla)
230	0	127.1	27.1	6.89	3.18	4.80	713	−40.99(223)	3.47(19)
230	20.7	135.7	31.0	7.12	3.40	5.04	682	−43.40(201)	3.84(18)
245	0	136.6	31.6	7.14	3.43	5.07	676	−42.99(186)	3.84(17)
245	20.7	145.8	35.9	7.38	3.66	5.32	647	−41.66(234)	3.89(22)
260	0	146.1	36.2	7.38	3.67	5.33	644	−41.23(201)	3.87(19)
260	20.7	156.0	41.2	7.63	3.92	5.59	616	−34.06(218)	3.34(21)

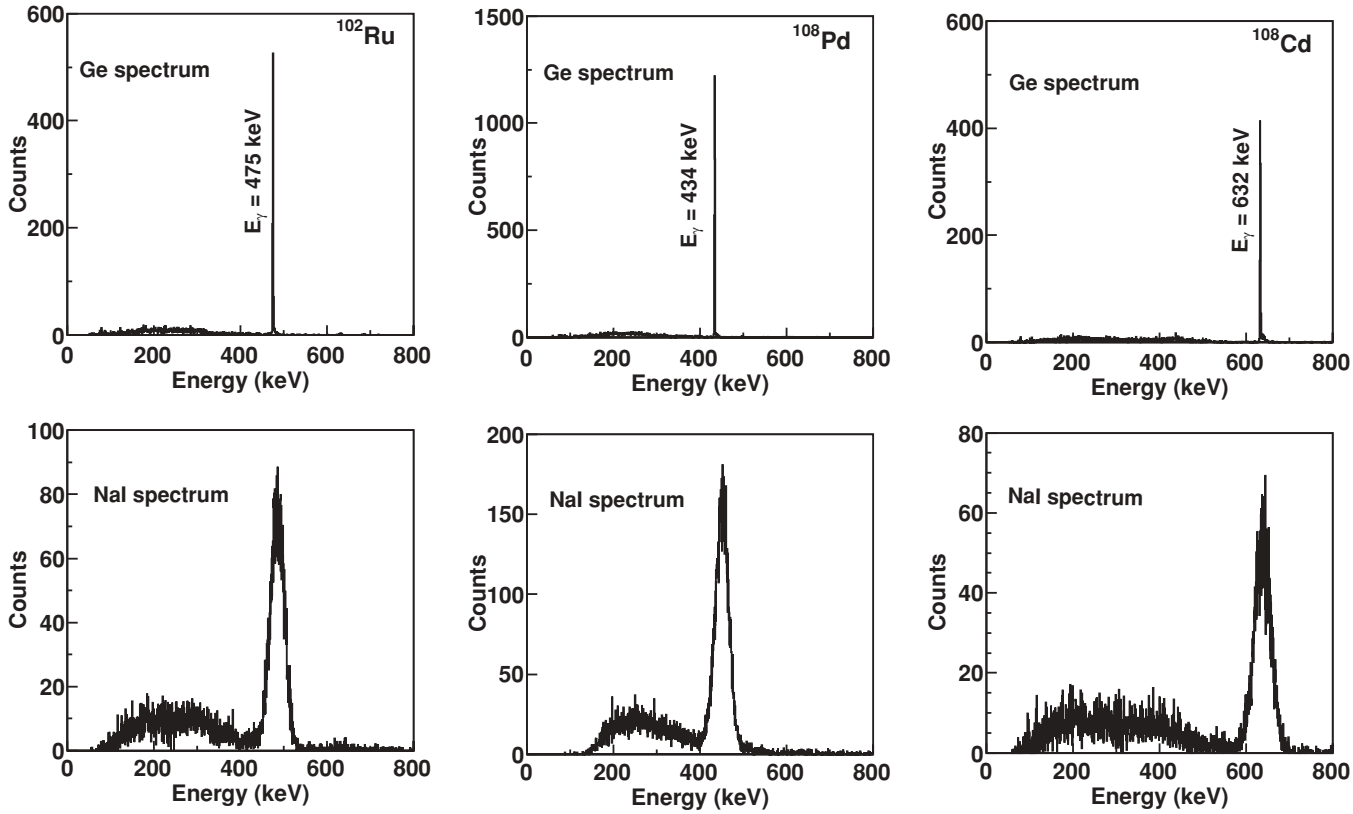

FIG. 5. Examples of γ-ray spectra observed at $+65^\circ$ and $+115^\circ$ to the beam axis in coincidence with C ions forward scattered into the outer-particle counters. These spectra represent all of the data for the field-up direction, obtained during the precession measurements on ^{102}Ru, ^{108}Pd, and ^{108}Cd using Target II.

parametrization to determine the scaling ratios described in Sec. II, which are needed to correct for differences in the velocity range over which the different isotopes experience the transient field.

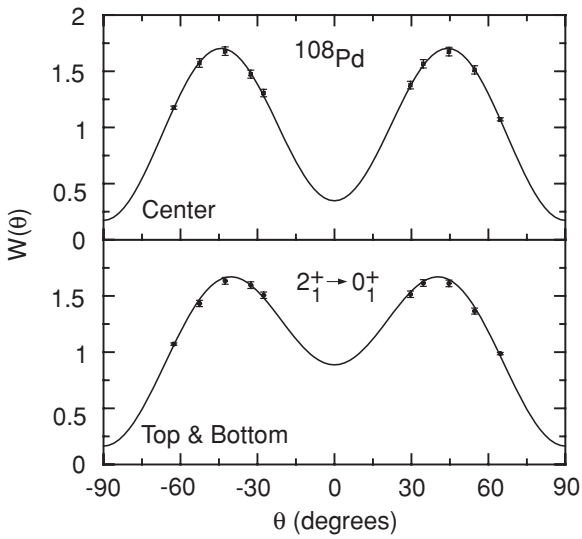

FIG. 6. Measured and calculated angular correlations for ^{108}Pd in inverse kinematics. The upper panel is for the center-particle detector (average ^{12}C scattering angle 0°); the lower panel is for the top and bottom (outer-) particle detectors (average ^{12}C scattering angle 20.7°).

The absolute scale of the experimental g factors has been set here by reference to previous measurements on ^{106}Pd by the external field and radioactivity techniques [26,27].

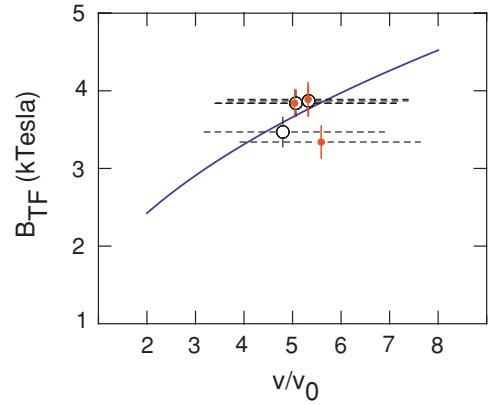

FIG. 7. (Color online) Measured transient-field strength for ^{108}Pd ions traversing the gadolinium layer of Target I. Dotted horizontal lines indicate the velocity range over which the transient field is sampled. The average transient-field strength is plotted at the average ion velocity. Open symbols correspond to the detection of ^{12}C ions in the central detector, while filled symbols indicate detection in the outer detectors with an average scattering angle of 20.7°. The solid line shows the $v^{0.45}$ velocity dependence of the Rutgers parametrization [19] scaled to best fit these data.

TABLE VII. Results of g-factor measurements in inverse kinematics. $\langle\Delta\Theta\rangle_{\rm obs}$ is the average observed experimental precession angle. The g factors are referenced to $g(2_1^+; {}^{106}\mathrm{Pd} = +0.393)$ and assigned uncertainties that reflect the uncertainties in the measured precession angles. Adopted g factors, which include uncertainties in the reference g factor, are presented in Sec. II C.

Nuclide	$\langle\Delta\Theta\rangle_{\rm obs}$ (mrad)	g
	Target I	
^{102}Ru	−50.68(148)	+0.436(13)
^{108}Pd	−42.48(146)	+0.347(12)
^{114}Cd	−41.43(175)	+0.313(14)
	Target II	
^{96}Ru	−40.94(223)	+0.440(24)
^{98}Ru	−40.18(217)	+0.414(22)
^{100}Ru	−42.95(136)	+0.431(14)
^{102}Ru	−45.01(191)	+0.449(19)
^{104}Ru	−44.20(138)	+0.436(14)
^{102}Pd	−43.84(196)	+0.418(19)
^{104}Pd	−48.12(140)	+0.461(14)
^{106}Pd	−41.19(92)	+0.393(9)
^{108}Pd	−36.79(126)	+0.347(12)
^{110}Pd	−37.23(119)	+0.350(11)
^{106}Cd	−43.08(228)	+0.393(21)
^{108}Cd	−42.02(220)	+0.389(20)
^{112}Cd	−39.80(232)	+0.365(21)
	Target III	
^{98}Mo	−30.42(223)	+0.459(34)
^{96}Ru	−29.70(169)	+0.432(24)
^{100}Ru	−29.89(141)	+0.411(20)
^{102}Ru	−31.21(97)	+0.428(14)
^{104}Ru	−26.99(150)	+0.369(14)
^{106}Pd	−30.03(148)	+0.393(20)

We have followed the recommendation of Johansson *et al.* [26] and disregarded the measurements that used iron hosts, which gave evidence of having slightly reduced hyperfine fields. The adopted g factor is then the weighted average of their measurement using a cobalt host [26] and an earlier external field measurement with which it agrees [27]. After making a small correction for a more recent level lifetime [$\tau = 17.6(9)$ ps [20]], we obtain $g = +0.393(23)$, with the uncertainty dominated by the uncertainty in the lifetime. The most recent nuclear data evaluation [28] for ^{106}Pd includes iron-host data [29,30]. If these data are included in the average (after being adjusted to correspond to the same adopted lifetime), the resultant value $g = +0.378(21)$ is smaller than, but remains consistent with, our adopted value.

Precession and g-factor results are summarized in Table VII. Figure 8 shows a comparison of the present and previous data for relative g factors in the Pd isotopes. The previous measurements used the transient-field technique in conventional kinematics, whereas the present measurements use inverse kinematics. The consistency of the data in Fig. 8 is important because transient-field measurements in inverse kinematics, such as those reported here, are reaching a high level of statistical precision, to the point where uncontrolled systematic effects associated with changing the beam species might become evident.

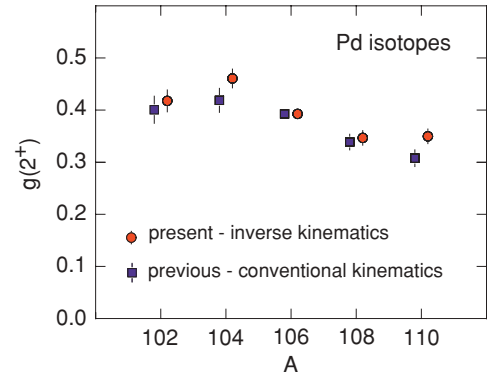

FIG. 8. (Color online) Comparison of transient-field measurements on the Pd isotopes. The present measurements in inverse kinematics are compared with previous measurements in conventional kinematics [31–34]. The data are shown relative to the present adopted $g(2^+)$ value in ^{106}Pd.

C. Adopted g factors

This section gives a summary of the present and previous $g(2_1^+)$ values in Mo, Ru, Pd, and Cd isotopes.

Table VIII summarizes the previous data on the Mo isotopes from Refs. [7,12], along with the values adopted for the following comparison with theory. The new measurement for $g(2_1^+)$ in ^{98}Mo, relative to ^{106}Pd, is included in the summary of adopted g factors.

Table IX summarizes the g factors in the Ru isotopes. Further explanation is required concerning the method used to combine the results of the three independent sets of measurements on the Ru isotopes (one in conventional kinematics and two in inverse kinematics). On one hand, the two measurements in inverse kinematics with gadolinium as the ferromagnetic host were calibrated relative to measurements on ^{106}Pd (and ^{98}Mo) performed with the same target. On the other hand, the measurement in conventional kinematics,

TABLE VIII. $g(2_1^+)$ values in the Mo isotopes.

Nuclide	$g(2^+)$		
	Previous	Present	Adopted
^{92}Mo	+1.15(14)[a]		+1.15(14)
^{94}Mo	+0.308(43)[a]		+0.308(43)
^{96}Mo	+0.394(31)[a]		+0.394(31)
^{98}Mo	+0.483(36)[a]	+0.485(29)	+0.485(29)
^{100}Mo	+0.471(33)[a]		+0.471(33)
^{102}Mo	+0.42(7)[b]		+0.42(7)
^{104}Mo	+0.27(2)[c]		+0.27(2)
^{106}Mo	+0.21(2)[c]		+0.21(2)
^{108}Mo	+0.5(3)[c]		+0.5(3)

[a]Adopted value in [12].
[b]Reference [36].
[c]Reference [7].

TABLE IX. $g(2_1^+)$ values in the Ru isotopes.

Nuclide	$g(2^+)$		
	Previous	Present	Adopted
^{96}Ru		+0.445(28)	+0.445(28)
^{98}Ru	+0.4(3)[a]	+0.408(32)	+0.408(32)
^{100}Ru	+0.46(5)[b]	+0.429(23)	+0.429(23)
^{102}Ru	+0.37(8)[b]		
	+0.354(21)[c]	+0.453(23)	+0.453(23)
^{104}Ru	+0.41(5)[a]	+0.406(21)	+0.406(21)
^{106}Ru	+0.28(13)[d]		+0.28(13)[e]
^{108}Ru	+0.28(4)[d]		+0.28(4)[e]
^{110}Ru	+0.42(6)[d]		+0.42(6)[e]
^{112}Ru	+0.44(9)[d]		+0.44(9)[e]

[a]From [37].
[b]From [35], updated for lifetime in [20].
[c]From [26], updated for lifetime in [20].
[d]From [7].
[e]As discussed in the text, there may be evidence that these values should be increased by a factor of 1.2.

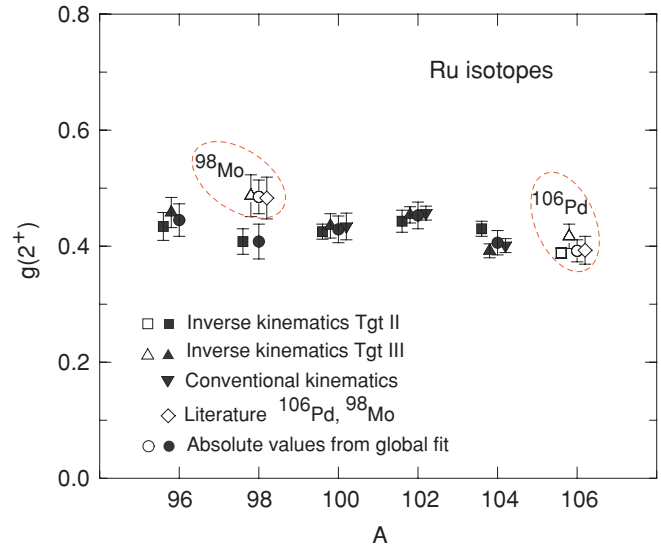

FIG. 9. (Color online) Comparison of g factors from the three measurements on the Ru isotopes, calibration values from the literature, and the average values obtained from the global fit. See text.

with an iron host, was calibrated (Sec. II A2) using the Rutgers parametrization [19]. In this situation, it is difficult to properly combine the data sets and propagate the errors by the usual procedure of working with one or two g-factor ratios. Nevertheless, the mathematical relationships relating the data sets are simple.

The procedure adopted to combine these measurements began by writing down the relationships between all of the experimental "knowns," namely, the measured precession angles and previously determined g-factor values, and the experimental "unknowns," i.e., the transient-field strengths and the g factors to be extracted from the data. To illustrate the procedure, it is most convenient to work with corrected experimental precession angles $\Delta\Theta(A)$, as defined in Eq. (5), and the integral transient-field strengths $\phi(\infty)$, as defined in Eq. (4). The six precession measurements on Target II are then related by $\Delta\Theta_{\rm II}(A) = g(A)\phi_{\rm II}$, where A denotes the six even-even nuclei $^{96-104}$Ru and ^{106}Pd; $\phi_{\rm II}$ is the same for all measurements on Target II. Similarly, the six precession measurements on Target III are related by $\Delta\Theta_{\rm III}(A) = g(A)\phi_{\rm III}$, where A now denotes $^{96,100-104}$Ru, ^{98}Mo, and ^{106}Pd. The three experimental precessions measured in conventional kinematics are related by $\Delta\Theta_{\rm conv}(A) = g(A)\phi_{\rm conv}$, where A denotes $^{100-104}$Ru. With these data alone, only ratios of g factors can be obtained. Additional data must be used to obtain the absolute values of the g factors or, alternatively, the values of $\phi_{\rm II}$, $\phi_{\rm III}$, and $\phi_{\rm conv}$. As noted above, for this purpose, we have used the previously measured g factors in both ^{106}Pd and ^{98}Mo, along with the Rutgers parametrization [19] to determine $\phi_{\rm conv}$. The parametrization of the field strength, and hence $\phi_{\rm conv}$, was assigned a 10% uncertainty (i.e., $a_{\rm TF} = 16.9 \pm 1.7$ T in Eq. (3)).

The set of equations relating the experimental precessions, the g factors, the integrated transient-field strengths, and the previous data to be used for field calibration were then used as the basis for a χ^2 fit to determine the Ru g factors. The fitting procedure gives the correct average values for the Ru g factors and their associated experimental uncertainties, including the uncertainty in the transient-field calibration.

The fit included the precession data for all three measurements, the previous experimental g factors in ^{106}Pd and ^{98}Mo, and the scale parameter of the transient field for the Rutgers parametrization applied to iron hosts. There were, therefore, 18 data values in the fit (15 $\Delta\Theta$ values, two independently measured g factors, and one transient-field scale factor). Ten parameters were extracted from the fit: the five g factors for the even Ru isotopes between ^{96}Ru and ^{104}Ru, the transient-field strengths in the three measurements, and the g factors of ^{106}Pd and ^{98}Mo. Note that new values of the latter two g factors were output fit parameters while their previous experimental values were input data for the fit.

TABLE X. $g(2_1^+)$ values in the Pd isotopes. Uncertainties in square brackets are relative errors for the sequence of isotopes; errors in parentheses include the uncertainty in the transient-field calibration.

Nuclide	$g(2^+)$		
	Previous	Present	Adopted
^{102}Pd	+0.401 [26][a]	+0.418[21]	0.411(30)
^{104}Pd	+0.419 [0.23][a]	+0.461[18]	0.446(30)
^{106}Pd	+0.393 [0][a]	+0.393[0]	0.393(23)
^{108}Pd	+0.339 [15][a]	+0.347[14]	0.343(22)
^{110}Pd	+0.308 [16][a]	+0.350[14]	0.333(21)
^{112}Pd			
^{114}Pd	+0.24(13)[b]		+0.24(13)
^{116}Pd	+0.2(1)[b]		+0.2(1)

[a]Average of relative g-factor measurements in [31–34], normalized to the adopted value for ^{106}Pd.
[b]From [7]. The result for ^{114}Pd corresponds to $\tau = 117(6)$ ps [38,39].

TABLE XI. $g(2_1^+)$ values in the Cd isotopes.

Nuclide	$g(2^+)$	
	Previous[a]	Present and adopted
^{106}Cd	0.40(10)	+0.393(31)
^{108}Cd	0.34(9)	+0.389(31)
^{110}Cd	0.285(55)[b]	+0.407(29)
^{112}Cd	0.32(8)	+0.360(24)
^{114}Cd	0.29(7)	+0.325(21)
^{116}Cd	0.30(7)	+0.296(24)

[a]From [31].
[b]Calibration value adopted in [31].

The χ^2 per degree of freedom was 0.95. The results of this fit procedure and the consistency of the three data sets are shown in Fig. 9. The field calibration, and hence the absolute values of the g factors, was determined predominantly by the previous g factor in ^{106}Pd. Indeed, the value of $g(2^+)$ in ^{106}Pd returned by the fit did not differ significantly in either magnitude or precision from the adopted previous value. For ^{98}Mo, however, an improved $g(2^+)$ value was obtained and is reported in Table VIII. It is worth noting that the transient field strength for Ru in iron hosts agreed with the Rutgers parametrization [19] to within 5%, whereas, for the measurements on gadolinium hosts, the transient field strength was of order 30% stronger than the prediction of the Rutgers parametrization.

As can be seen from Table IX, the present g factor for ^{102}Ru is 20% higher than that obtained by Johansson *et al.* from perturbed angular correlation measurements on a radioactive source alloyed with an iron host [26]. They assumed a static hyperfine field of $B_{\rm hf} = 50.3 \pm 0.9$ T. Their paper discusses at length, however, the possible processes that introduce systematic errors in this type of measurement, which usually cause a reduction in the effective hyperfine field. The present g-factor measurement implies that, in Ref. [26], the effective static field for Ru impurities in iron was $B_{\rm hf} = -40 \pm 3$ T. Our results are in better agreement with the radioactivity measurements of Auerbach *et al.* [35], who took $B_{\rm hf} = -44 \pm 3$ T.

Smith *et al.* [6,7] adopted a hyperfine field for Ru in iron of $B_{\rm hf} = -47.8 \pm 0.1$ T. The above discussion suggests that this may be an overestimate. However, aside from noting that there may be grounds to increase the previously reported g factors of the neutron-rich isotopes [6,7] by about 20%, these values are reported without adjustment in Table IX.

Finally, it is to be noted that Taylor *et al.* [25] performed transient-field g-factor measurements on the Ru isotopes in parallel with this work. Their adopted g factors agree within the experimental uncertainties with those reported here. Tables X and XI summarize the previous, present and adopted g factors for the Pd and Cd isotopes.

III. TIDAL-WAVE APPROACH FOR g-FACTOR CALCULATIONS

As noted in the Introduction, the tidal-wave model uses the fact that, in the semiclassical approximation, the yrast states of vibrational nuclei correspond to quadrupole waves traveling over the surface of the nucleus, like the tidal waves over the surface of the ocean. In the frame of reference that co-rotates with the wave, the quadrupole deformation is static, like that of a rotor. The difference between the vibrator and rotor is that the angular momentum of an ideal rotor is generated by increasing the angular velocity, whereas in the case of the ideal vibrator, the angular velocity is constant (equal to half the vibrational frequency) and angular momentum is generated by increasing the amplitude of the wave. Real nuclei are in-between these idealized limits, i.e., both deformation and angular velocity increase with angular momentum. The fact that the yrast states of vibrational, transitional, and rotational nuclei correspond, in the semiclassical approximation, to a uniformly rotating statically deformed shape allows the use of the self-consistent cranking model for describing yrast states in transitional nuclei. It was demonstrated in Refs. [8,9] that the energies of the yrast states in even-even nuclei with $44 \leqslant Z \leqslant 48$ and $54 \leqslant N \leqslant 68$ are very well described by this model. Individual differences between the nuclides, which reflect the response of the nucleonic orbits at the Fermi surface to rotation, are reproduced. The $B(E2)$ values of the transitions between the yrast levels are also well accounted for, including their linear increase with angular momentum in vibrational nuclei. In this section, the extension of the model to calculate g factors is described.

The details of the tidal-wave approach are presented in Refs. [8,9]. In essence, the self-consistent cranking model is applied to nuclei that are spherical or weakly deformed in their ground states. The calculations are based on the tilted-axis-cranking (TAC) version of the cranking model as described in Ref. [40]. The cases considered correspond to a rotation of the nucleus about a principal axis. We start from the rotating mean field

$$h' = h_{\rm Nilsson}(\epsilon, \gamma) + \Delta(P^+ + P) - \omega J_x - \lambda N, \qquad (7)$$

which consists of quadrupole deformed Nilsson potential $h_{\rm Nilsson}$ [41], combined with a monopole pair field P^+ and fixed pair potential Δ. The chemical potential λ is fixed for each deformation such that the particle number is correct for $\omega = 0$.

The calculations of the g factors are performed on a grid of triaxial quadrupole deformations while the angular frequency ω is fixed at every grid point by the condition

$$J = \langle \omega(J)|J_x|\omega(J)\rangle + J_c, \qquad (8)$$

which is facilitated by linear interpolation between discrete ω grid points. A small correction is applied to the angular momentum

$$J_c = 100\ {\rm MeV}^{-1}\varepsilon_2^2 \sin^2(\gamma - \pi/3)\omega. \qquad (9)$$

About half of it takes into account the coupling between the oscillator shells and another half is expected to come from quadrupole pairing, both being neglected in the cranking calculations. For the study of the 2_1^+ states, $J = 2$ was set. The calculations for $J = 4$ have also been carried out. The diabetic tracing technique, as described in Ref. [40], reliably prevented sudden changes of the quasiparticle configuration. The tracing

was performed by using moderate steps $\Delta\omega = 0.05$ MeV and comparing the overlap of configurations step by step.

The total energies are calculated by means of the Strutinsky method (SCTAC in [40])

$$E(J,\epsilon,\gamma) = E_{LD}(\epsilon,\gamma) - \tilde{E}(\epsilon,\gamma) + \langle\omega(J)|h'|\omega(J)\rangle - \langle\omega = 0|h'|\omega = 0\rangle + \omega(J)J. \quad (10)$$

After minimizing the energy $E(J,\epsilon,\gamma)$ to obtain the equilibrium deformation parameters ϵ_e and γ_e, the magnetic moment is calculated:

$$\mu = \langle\omega(J),\epsilon_e,\gamma_e|\mu_x|\omega(J),\epsilon_e,\gamma_e\rangle, \quad (11)$$

where

$$\mu_x = \mu_N[J_{x,p} + (\eta 5.58 - 1)S_{x,p} - \eta 3.73 S_{x,n}]. \quad (12)$$

The spin contributions to the single-particle magnetic moments were evaluated with a common attenuation factor $\eta = 0.7$. The possibility that the correction term to the angular momentum J_c contributes to the magnetic moment was disregarded. The g factor is given by

$$g(J) = \frac{\mu(J)}{J}. \quad (13)$$

The g factors turned out to be sensitive to the choice of Δ_p and Δ_n. (See, e.g., Ref. [42] for a general discussion on the sensitivity of g factors to pairing.) For the transitional nuclei around $A = 100$, the experimental pairing parameters Δ, as calculated from the even-odd mass differences, fluctuate considerably with the particle numbers. Using these experimental values in the calculations translates into fluctuations of the g factors that are in contradiction to experiment. The even-odd mass differences do not only reflect the pairing strength, but are also sensitive to the level spacing and deformation changes, which may be the major source of the fluctuations. For this reason, we adopted constant values of Δ, which are somewhat smaller than the average experimental values obtained by means of the four-point formula. The pair gap parameters $\Delta_p = \Delta_n = 1.1$ MeV are adopted for the Mo and Ru isotopes and $\Delta_p = \Delta_n = 1.2$ MeV for the Pd and Cd isotopes. The results for $\Delta_p = \Delta_n = 1.1$ MeV are also shown for several Pd and Cd isotopes.

In all cases, we have reported g factors for the nuclear deformation of minimum calculated energy. For the heaviest isotopes of Mo and Ru, the Strutinsky method predicts that the oblate minimum is lowest, with a close-by prolate minimum. As with other mean-field approaches, the inaccuracies in the prolate-oblate energy difference are of the order of a few hundred keV. In both ^{108}Mo and ^{112}Ru, there are small energy differences along the gamma degree of freedom. A detailed examination of the dependence of the g factors on the nuclear shape in such cases is beyond the scope of this paper. The effect is expected to be secondary compared to the effects of pairing, which affects the calculated shapes as well as the g factors.

The results of the calculations are listed in Table XII and compared with the experimental data in Fig 10. By applying the same calculation, the energies, $B(E2)$ values, and g factors can be obtained for the yrast sequences in the considered nuclei (see also Refs. [8,9]). The good agreement with experimental data demonstrates the applicability of the tidal-wave approach.

TABLE XII. Deformations and calculated g factors.

Nuclide	Deformation 0^+		Deformation 2^+		$g(2^+)$	$g(4^+)$
	ϵ_2	γ	ϵ_2	γ		
$^{92}_{42}$Mo$_{50}$	0.000	0	0.000	0	1.323	
$^{94}_{42}$Mo$_{52}$	0.001	5	<0.090	0	0.583	
$^{96}_{42}$Mo$_{54}$	0.008	5	0.117	0	0.491	
$^{98}_{42}$Mo$_{56}$	0.169	25	0.165	0	0.528	
$^{100}_{42}$Mo$_{58}$	0.199	25	0.198	0	0.416	
$^{102}_{42}$Mo$_{60}$	0.231	25	0.239	15	0.357	
$^{104}_{42}$Mo$_{62}$	0.252	20	0.256	15	0.305	
$^{106}_{42}$Mo$_{64}$	0.260	15	0.260	15	0.300	
$^{108}_{42}$Mo$_{66}$	−0.225	0	−0.228	0	0.334	
$^{96}_{44}$Ru$_{52}$	0.128	0	0.130	0	0.615	
$^{98}_{44}$Ru$_{54}$	0.119	0	0.120	0	0.533	
$^{100}_{44}$Ru$_{56}$	0.125	0	0.130	0	0.550	0.468
$^{102}_{44}$Ru$_{58}$	0.150	0	0.151	0	0.470	0.209
$^{104}_{44}$Ru$_{60}$	0.175	0	0.176	0	0.350	0.145
$^{106}_{44}$Ru$_{62}$	0.200	0	0.200	0	0.324	0.194
$^{108}_{44}$Ru$_{64}$	0.210	0	0.210	0	0.310	0.193
$^{110}_{44}$Ru$_{66}$	0.210	0	0.211	0	0.350	0.231
$^{112}_{44}$Ru$_{68}$	−0.210	0	−0.210	0	0.301	
$^{102}_{46}$Pd$_{56}$	0.100	0	0.120	0	0.405	0.611
$^{104}_{46}$Pd$_{58}$	0.125	0	0.135	0	0.425	0.504
$^{106}_{46}$Pd$_{60}$	0.126	0	0.150	0	0.350	0.320
$^{108}_{46}$Pd$_{62}$	0.150	0	0.151	0	0.303	0.204
$^{110}_{46}$Pd$_{64}$	0.152	0	0.154	0	0.270	0.186
$^{112}_{46}$Pd$_{66}$	0.154	0	0.156	0	0.259	0.222
$^{114}_{46}$Pd$_{68}$	0.190	0	0.191	0	0.241	
$^{116}_{46}$Pd$_{70}$	0.174	0	0.170	0	0.239	
$^{104}_{48}$Cd$_{56}$	0.000	0	0.090	0	0.331	0.288
$^{106}_{48}$Cd$_{58}$	0.050	0	0.100	0	0.314	0.327
$^{108}_{48}$Cd$_{60}$	0.075	0	0.114	0	0.302	0.163
$^{110}_{48}$Cd$_{62}$	0.050	0	0.100	0	0.297	0.142
$^{112}_{48}$Cd$_{64}$	0.000	0	0.120	0	0.212	0.125
$^{114}_{48}$Cd$_{66}$	0.050	0	0.117	0	0.174	0.117
$^{116}_{48}$Cd$_{68}$	0.070	0	0.090	0	0.161	
$^{118}_{48}$Cd$_{70}$	0.100	0	0.110	0	0.178	

IV. DISCUSSION

A. g factor trends in the tidal-wave model

The N dependence of g factors in transitional nuclei has been a challenge to theory. The main reason is that the g factors are sensitive to the underlying single-particle composition of the collective quadrupole degree of freedom. The collective states of transitional nuclei have been mostly described in the framework of phenomenological collective models such as the Bohr Hamiltonian [1] and the interacting boson model (IBM) [2], which do not specify the fermionic structure of the collective mode. On this level, one simply assumes that only the protons are responsible for the current that generates the magnetic moment, i.e., $g = Z/A$. Sambataro and Dieperink [43] addressed the experimental deviations of the g factors of the transitional isotopes of Ru to Te in the framework of the proton-neutron interacting boson model. Since then, there

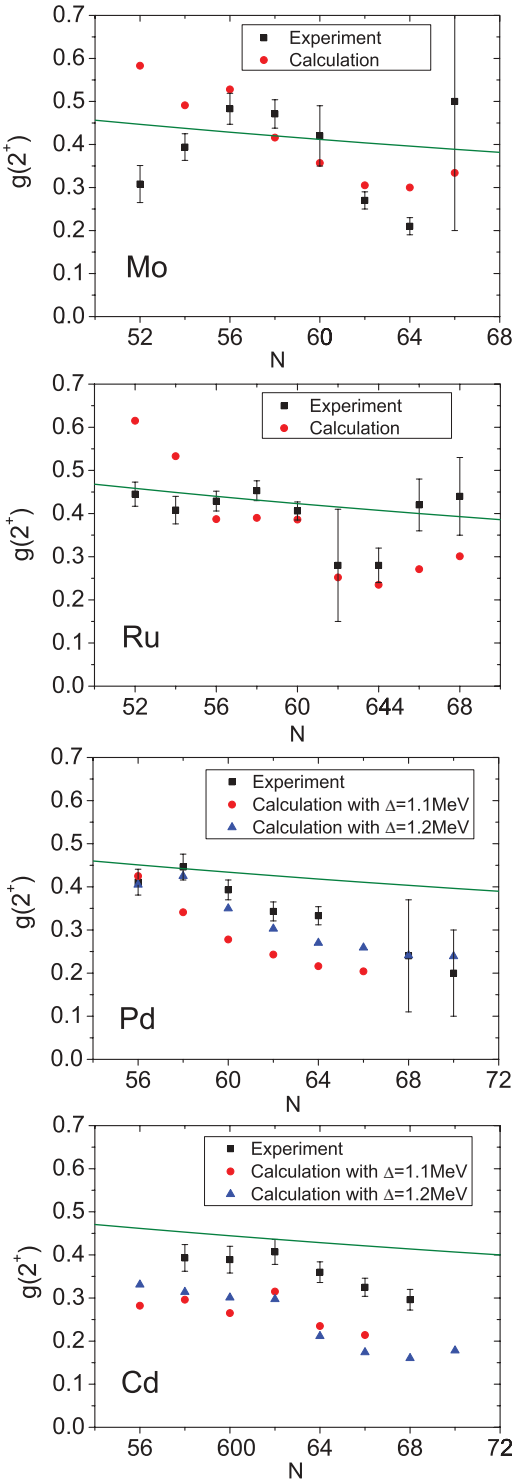

FIG. 10. (Color online) $g(2^+)$ calculations compared with experiment. The green line shows Z/A.

has been little progress toward a deeper microscopic-based interpretation. We approach the problem anew within the tidal-wave model [8,9], which is completely microscopic. It describes the yrast states by means of the self-consistent cranking model, which allows one to calculate the magnetic moment directly from the nucleonic currents. In applying it to nuclei that are spherical or slightly deformed in their ground state, one has to numerically diagonalize the quasiparticle Routhian [Eq. (7)]. Only for well-deformed nuclei is the perturbative expression, as given in Ref. [44], applicable. The calculations in Refs. [8,9] indicate that the nuclides in the considered transitional region are anharmonic vibrators or very soft rotors. The deformation of the 2^+ state increases with the number of valence proton holes below, and neutron particles above, the $Z = N = 50$ shell. It ranges from $\epsilon_2 \sim 0.1$ for the vibrational Cd isotopes to ~0.25 for the rotational nuclei ^{102,104,106}Mo. For each isotope chain, the deformation increases with the neutron number. Figure 10 shows that the calculated g factor trends are in overall good agreement with experiment. In particular, the deviations from the value Z/A are well accounted for.

The Z and N dependence of the g factors will now be discussed. Looking at the microscopic contributions to the angular momentum, it is seen that a few quasiparticle levels near the Fermi surface contribute most to the total angular momentum. The g factors generally decrease along the isotope chains. This decrease is the result of the fractional increase of J_{n5}, the angular-momentum contribution from the $h_{11/2}$ neutrons. To elucidate this observation, Fig. 11 compares the calculated g factors with the simple approximation

$$g(J) \approx \left(1.43 J_{p4} - 0.24 J_{n5}\right)/2, \tag{14}$$

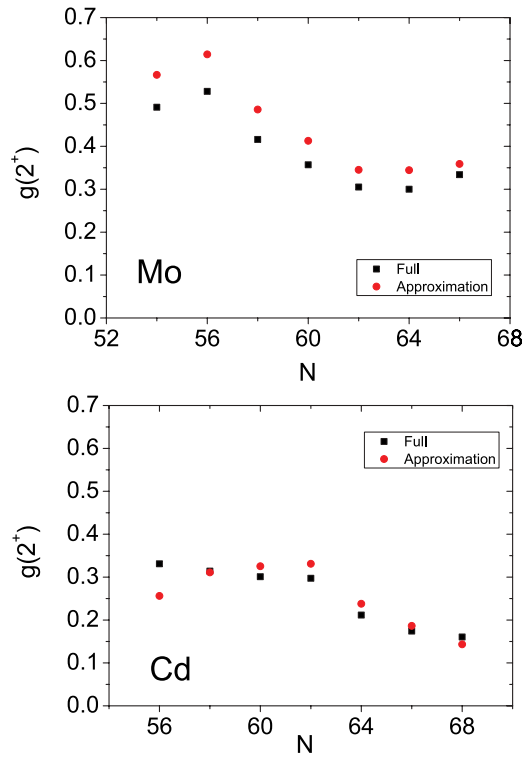

FIG. 11. (Color online) Comparison between calculated g factors. Black squares show the full calculation as described in the text and shown in Fig. 10. Red dots show the approximation of Eq. (14), which takes into account only the magnetic moments generated by the $g_{9/2}$ protons and the $h_{11/2}$ neutrons.

where J_{p4} and J_{n5} are the angular momenta calculated by means of the cranking model for the proton $N = 4$ and the neutron $N = 5$ shells, respectively. This approximation assumes that (i) only the $g_{9/2}$ proton holes and the $h_{11/2}$ neutrons contribute to the magnetic moment, and (ii) the expression

$$g = g_l \pm \eta \frac{g_s}{2l+1}, \tag{15}$$

which is valid for the spherical shells, can be used to set the nucleon g factors. The contribution from the neutron $N = 4$ shell is assumed to be zero because it is generated by the $d_{3/2}$ and $d_{5/2}$ orbitals, which have opposite g factors. Figure 11 compares the approximation of Eq. (14) with the full calculation. It is seen that the approximation qualitatively accounts for the N dependence of the g factors. The separate contributions of the various oscillator shells N to the total magnetic moment were calculated by means of Eq. (12). It turned out that the contributions of the $N = 3$ proton and neutron shells, and of the $N = 4$ neutron shell, are negligible. The errors of the approximation in Eq. (14) are therefore due to the use of the single-nucleon g factors for spherical j shells. Nevertheless, the simplified expression [Eq. (14)] allows one to understand the N and Z dependence of the excited-state g factors.

As an example, the behavior of the Mo isotopes was examined in greater detail. Figure 12 shows the composition of the angular momentum of the 2^+ state. With increasing numbers of valence neutrons, the $g_{9/2}$ proton fraction J_{p4} remains nearly constant for the isotope chain, whereas the $h_{11/2}$ neutron fraction J_{n5} increases, which causes the decrease of the g factor. As illustrated in Fig. 13, the increased neutron numbers push up the Fermi surface and, with increased deformations, the Fermi level moves into the lower half of the Nilsson orbits with $h_{11/2}$ parentage, which generate J_{n5}. Since the $h_{11/2}$ neutrons have $g = -0.24$, they progressively reduce the magnetic moment. In the Cd isotopes, the proton fraction J_{p4} is smaller because there are only two $g_{9/2}$ holes. The progressive occupation of the $h_{11/2}$ neutron orbitals generates the J_{n5} fraction seen in Fig. 12, which causes the decrease of the g factor clearly seen in Fig. 11 for the simplified expression [Eq. (14)].

For the Cd isotopes, the deformation of the 2^+ state is about 0.1. As seen in Fig. 13, the Fermi level reaches the $h_{11/2}$ states only at $N = 64$. However, one has to keep in mind that the smaller deformation implies a higher angular frequency of the tidal wave, which lowers the $h_{11/2}$ orbitals relative to the positive parity orbitals. For this reason, the occupation of the $h_{11/2}$ orbitals starts already at $N = 60$. Hence, in the studied region, the neutrons in the $h_{11/2}$ orbit are primarily responsible for the drop of the g factors with increasing neutron number. This observation agrees with the inference of Smith *et al.* [6] based on their measured g factors for several neutron-rich isotopes. Moreover, it has long been known that the strong increase of J_n in well-deformed nuclei, caused by the rotational alignment of the $i_{13/2}$ and $j_{15/2}$ neutrons, reduces the g factors below Z/A [45].

The g factors of the Cd isotopes are underestimated by about 20%. Reducing the proton pair gap Δ_p by about 10%,

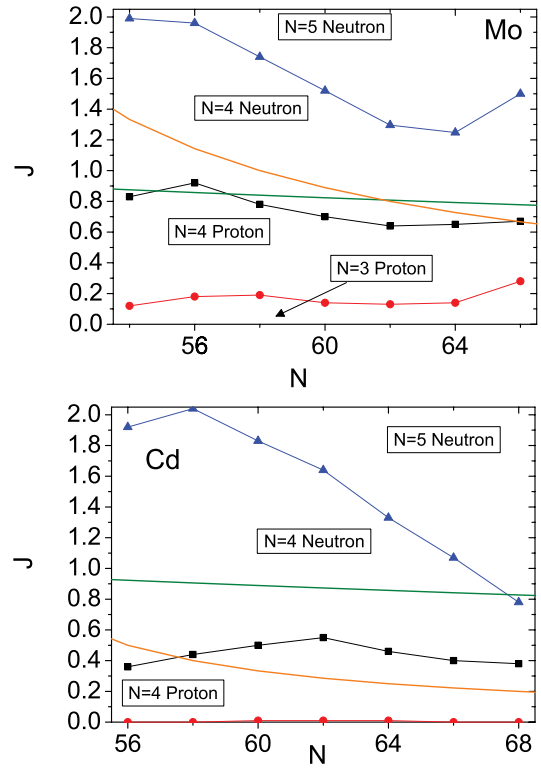

FIG. 12. (Color online) Composition of the angular momentum of the 2^+ states of the Mo and Cd isotopes. The fraction of $J = 2$ of each oscillator shell as obtained from the cranking model is shown. The distance between the lower frame and the circles (red curve) is the fraction of the protons in the $N = 3$ oscillator shell, the distance between the circles and squares (red and black curves) the $N = 4$ proton fraction, the distance between the squares and triangles (black and blue curves) the $N = 4$ neutron fraction, and the distance between the triangles (blue curve) and the upper frame the $N = 5$ neutron fraction. The contribution of the $N = 5$ protons is negligible. The distance between the lower frame and orange curve with no symbols is the proton fraction according to the IBM-II boson counting rule calculated by means of Eq. (16). The neutron fraction is the distance between this curve and the upper frame. The straight green line shows $2Z/A$.

while keeping the neutron gap Δ_n unchanged, would increase the proton fraction J_p relative to the neutron fraction J_n, such that the g factors have the correct magnitude. The N-dependent trend will not be changed. A reduced Δ_p for $Z = 48$ appears reasonable because there are only two proton holes to generate pair correlations. The other isotopes have more proton holes, which generate stronger pair correlations.

The "canonical" estimate $g = Z/A$ for collective quadrupole excitations is based on the assumptions that (i) the ratio $J_p/(J_p + J_n) = Z/A$ and (ii) the spin contributions of the protons and neutrons cancel. Assumption (i) is rather poor for the Cd isotopes, which are almost semi-magic. It becomes better for Mo isotopes, which are situated further into the open shells. Assumption (ii) is not justified for the high-spin intruder orbitals $g_{9/2}$ and $h_{11/2}$, which almost completely generate the magnetic moment. Although (i) and (ii) become more valid assumptions for increasing numbers of valence nucleons, the

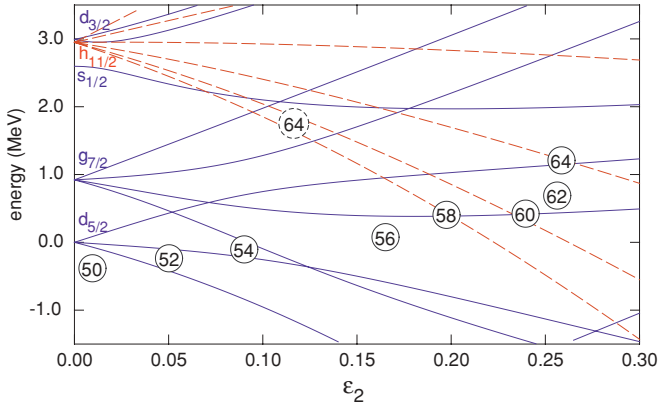

FIG. 13. (Color online) Nilsson diagram of molybdenum neutrons close to the $N = 50$ shell; the dashed lines represent negative parity and belong to $h_{11/2}$ levels. The neutron numbers of Mo isotopes are shown at the calculated equilibrium deformation, which illustrates the intrusion of the $h_{11/2}$ shell among the positive-parity orbits for $N < 64$, and explains the impact of $h_{11/2}$ orbit on the calculated g factors.

differences between the g factors of the nucleonic orbitals near the Fermi surface remain noticeable in the Z and N dependence of nuclear g factors (cf. Ref. [45]).

B. $N = 50, 52$ cases: ^{92,94}Mo, ^{96}Ru

The tidal-wave approach does not work for the $N = 50$ spherical nucleus ^{92}Mo. The ground-state configuration is not able to generate enough angular momentum to reach $J = 2$. By recognizing the fact that the neutrons of ^{92}Mo complete a shell, the lowest 2^+ configuration is obtained as the two-quasiproton configuration with angular-momentum projection of 2. Its deformation is found to be zero. The calculated g factor of 1.32 is close to the value 1.43 for the spherical $g_{9/2}$ proton orbital. The $N = 52$ nuclide ^{94}Mo also turns out to be not quite amenable to the tidal-wave approach. Assuming a deformation of $\epsilon_2 = 0.09$, one can generate two units of angular momentum at a frequency that is consistent with the energy of the 2^+ state. However, this deformation is not stable and the equilibrium deformation lies at a smaller value. As seen in Fig. 12, $J_{p4} = 0.8$, which generates the magnetic moment. The neutron fraction $J_{n4} = 1.2$ contributes very little due to a cancellation of the single-neutron components, particularly the $d_{5/2}$ and $g_{7/2}$ orbits (see Fig. 13), which have single-particle moments of opposite sign. The resulting g factor of 0.58 is much larger than the experimental value of 0.31 ± 0.04.

Recently, Holt *et al.* [4] carried out shell-model calculations, finding $g \approx 0.2$. They state that J_{n4} originates mainly from the $d_{5/2}$ orbital. Assuming that our value of $J_{n4} = 1.2$ exclusively originates from the $d_{5/2}$ orbital and using $g(d_{5/2}) = -0.52$ from Eq. (15), one finds $g(2^+) = (1.43 \times 0.8 - 0.52 \times 1.2)/2 = 0.26$, which is close to experiment. As compared with the shell model, in our calculations only pairing and quadrupole correlations are taken into account. It seems that the quadrupole correlations are overestimated, which causes an increased g factor through admixtures of the $g_{7/2}$ orbital.

In the case of the $N = 52$ nuclide ^{96}Ru, the tidal-wave approach gives a finite value of $\epsilon_2 = 0.13$ and a good estimate for the frequency of the 2^+ state. The calculated g factor is too large for the same reason as for ^{94}Mo, however, the discrepancy is less, which is likely a consequence of the increasing configuration mixing with the number of valence nucleons and deformation.

C. g factors of the 4^+ states

The tidal-wave model can predict the g factors of higher excited yrast states above the 2^+ state, and a number of such predictions have been included in Table XII. Unfortunately, the experiments to measure these g factors are challenging and experimental data are scarce. To our knowledge, the only measurement to date is the very recent work by Gürdal *et al.* [46] on ^{106}Pd, where $g(4^+) = 0.44 \pm 0.09$ was obtained, relative to $g(2^+) = 0.393 \pm 0.023$. Within uncertainties, the experimental g-factor ratio is consistent with the present predictions. Similar experiments on the heavier isotopes such as ^{110}Pd could decisively detect if $g(4^+) < 0.5g(2^+)$ as predicted by the tidal-wave-model calculations.

D. Comparison with interacting boson model

This paper gives new insights into the relative angular momentum carried by protons and neutrons in the transitional nuclei near $A = 100$, which can be compared and contrasted with the detailed analysis of Sambataro and Dieperink [43] based on the interacting boson model. These workers studied the g factors in this region in the framework of IBM-II, which distinguishes between proton and neutron bosons. The model parameters were fitted to the energies and $B(E2)$ values of the lowest collective quadrupole excitations. They found that, to a good approximation, $J_p \propto N_p$ and $J_n \propto N_n$, where N_p and N_n are the number of proton and neutron bosons, respectively. According to the IBM-II counting rule, these numbers are equal to one half of the number of valence proton holes and one half of the number of valence neutrons relative to $Z = N = 50$, respectively, i.e., for $J = J_p + J_n = 2$, one has

$$J_p = 2\frac{N_p}{N_p + N_n} = 2\frac{50 - Z}{50 - Z + N - 50} = 2\frac{50 - Z}{N - Z}. \quad (16)$$

Sambataro and Dieperink assigned effective g factors to the proton and neutron valence systems $g_p(N_p)$ and $g_n(N_n)$, which were assumed to depend on N_p and N_n. Considering $g_p(N_p)$ and $g_n(N_n)$ as free parameters, they fitted experimental g factors. They found that the resulting $g_p(N_p)$ and $g_n(N_n)$ values change smoothly with the boson numbers, and claimed that they qualitatively correlate with the g factors of the valence neutrons and protons that constitute the collective quadrupole mode.

Figure 12 compares the IBM-II values of J_p and J_n with our values, which are also are generated by the valence particles and holes. As seen, the IBM-II does not track closely with the proton-neutron ratio of the angular momentum obtained from our microscopic calculation. More important, it does not provide any information about the composition of the proton and neutron fractions, which is decisive for the calculation of

the magnetic moments. These deficiencies are overcome by introducing effective N_p- and N_n-dependent boson g factors, which are then adjusted to the experiment. In contrast, our discussion above demonstrates that the N and Z dependence of the measured g factors is well understood in terms of the microscopic J_p and J_n fractions and *constant* g factors for the $g_{9/2}$ proton holes and $h_{11/2}$ neutrons.

V. CONCLUSION

The g factors of the first excited 2^+ states in all of the stable even isotopes of Mo, Ru, Pd, and Cd have been studied experimentally and theoretically. An extensive set of measurements, using variations of the transient-field technique, was completed to ensure that the data set is internally consistent, i.e., the relative $g(2_1^+)$ values are accurate both within and between the isotope chains. Absolute values of the g factors were set relative to $g(2_1^+)$ in ^{106}Pd. The experimental precision has been improved considerably.

The data have been compared in detail with the tidal-wave version of the cranking model. We conclude that the tidal-wave approach gives a convincing description of the mass-dependent g-factor systematics in vibrational and transitional nuclei. Moreover, the g factors reveal the proton-neutron composition of the collective quadrupole mode. In comparison with previous work in this region based on the proton-neutron interacting boson model (IBM-II), the tidal-wave model is more solidly based on the underlying single-particle structure. It is found that the simple IBM-II counting rule based on the valence proton fraction gives only a rough guide. In particular, the individuality of the valence nucleons (especially their single-particle g factors) must be considered explicitly.

Looking to the future, on the experimental side, it is feasible to test the spin-dependent predictions of the tidal-wave model in a number of cases. In terms of improving the theory, it has been noted that the g factors are very sensitive to the relative strength of neutron and proton pairing. More accurate predictions than those presented here will require a more sophisticated, self-consistent treatment of pairing.

ACKNOWLEDGMENTS

The authors are grateful to the academic and technical staff of the Department of Nuclear Physics (Australian National University) for their assistance. Alan Devlin is thanked for contributions to the data collection. Mike Taylor, Noémie Koller, and Gerfried Kumbartzki are thanked for making available Target III and for discussions. This work was supported in part by the Australian Research Council Discovery Scheme Grant No. DP0773273. S.F. and J.S. acknowledge support by the DoE Grant No. DE-FG02-95ER4093.

[1] A. Bohr and B. R. Mottelson, *Nuclear Structure* (W. A. Benjamin, Reading, Massachusetts, 1975), Vol. II.
[2] F. Iachello and A. Arima, *The Interacting Boson Model* (Cambridge University Press, Cambridge, 1987).
[3] P. E. Garrett, K. L. Green, and J. L. Wood, Phys. Rev. C **78**, 044307 (2008).
[4] J. D. Holt, N. Pietralla, J. W. Holt, T. T. S. Kuo, and G. Rainovski, Phys. Rev. C **76**, 034325 (2007).
[5] A. Ekström *et al.*, Phys. Rev. C **80**, 054302 (2009).
[6] A. G. Smith *et al.*, Phys. Lett. B **591**, 55 (2004).
[7] A. G. Smith *et al.*, J. Phys. G: Nucl. Part. Phys. **31**, S1433 (2005).
[8] S. Frauendorf, Y. Gu, and J. Sun, arXiv:0709.0254.
[9] S. Frauendorf, Y. Gu, and J. Sun, Int. J. Mod. Phys. E **20**, 465 (2011).
[10] A. E. Stuchbery, A. B. Harding, D. C. Weisser, N. R. Lobanov, and M. C. East (unpublished).
[11] A. E. Stuchbery, I. Morrison, L. D. Wood, R. A. Bark, H. Yamada, and H. H. Bolotin, Nucl. Phys. A **435**, 635 (1985).
[12] P. F. Mantica, A. E. Stuchbery, D. E. Groh, J. I. Prisciandaro, and M. P. Robinson, Phys. Rev. C **63**, 034312 (2001).
[13] K.-H. Speidel, O. Kenn, and F. Nowacki, Prog. Part. Nucl. Phys. **49**, 91 (2002).
[14] N. Benczer-Koller and G. J. Kumbartzki, J. Phys. G: Nucl. Part. Phys. **34**, R321 (2007).
[15] A. E. Stuchbery, A. Nakamura, A. N. Wilson, P. M. Davidson, H. Watanabe, and A. I. Levon, Phys. Rev. C **76**, 034306 (2007).
[16] M. C. East, A. E. Stuchbery, S. K. Chamoli, A. N. Wilson, H. L. Crawford, J. S. Pinter, T. Kibédi, and P. F. Mantica, Phys. Rev. C **79**, 024303 (2009).
[17] M. C. East, A. E. Stuchbery, S. K. Chamoli, J. S. Pinter, H. L. Crawford, A. N. Wilson, T. Kibédi, and P. F. Mantica, Phys. Rev. C **79**, 024304 (2009).
[18] N. Benczer-Koller, M. Hass, and J. Sak, Annu. Rev. Nucl. Sci. **30**, 53 (1980).
[19] N. K. B. Shu, D. Melnik, J. M. Brennan, W. Semmler, and N. Benczer-Koller, Phys. Rev. C **21**, 1828 (1980).
[20] S. Raman, C. W. Nestor, and P. Tikkanen, At. Data Nucl. Data Tables **78**, 1 (2001).
[21] J. F. Ziegler, J. P. Biersack, and U. Littmark, *The Stopping and Range of Ions in Solids*, Vol. 1 of *The Stopping and Ranges of Ions in Matter*, edited by J. F. Ziegler (Permagon, New York, 1985).
[22] M. P. Robinson, A. E. Stuchbery, E. Bezakova, S. M. Mullins, and H. H. Bolotin, Nucl. Phys. A **647**, 175 (1999).
[23] N. Benczer-Koller, G. Lenner, R. Tanczyn, A. Pakou, G. Kumbartzki, A. Piqué, D. Barker, D. Berdichevsky, and L. Zamick, Phys. Rev. C **40**, 77 (1989).
[24] A. E. Stuchbery, S. K. Chamoli, P. T. Moore, M. C. East, T. Kibédi, and A. N. Wilson (unpublished).
[25] M. J. Taylor *et al.*, Phys. Rev. C **83**, 044315 (2011).
[26] K. Johansson, E. Karlsson, L.-O. Norlin, R. Å. Windahl, and M. R. Ahmed, Nucl. Phys. A **188**, 600 (1972).
[27] K. Johansson, L.-O. Norlin, and G. Carlsson, Ark. Fys. **37**, 445 (1968).
[28] D. de Frenne and A. Negret, Nucl. Data Sheets **109**, 943 (2008).
[29] J. D. Bowman, E. N. Kaufmann, S. K. Bhattacherjee, and M. Levanoni, Phys. Rev. Lett. **20**, 1176 (1968).
[30] V. Singh, J. Phys. Soc. Jpn. **29**, 1111 (1970).

[31] J. M. Brennan, M. Hass, N. K. B. Shu, and N. Benczer-Koller, Phys. Rev. C **21**, 574 (1980).
[32] J. L. Thornton, B. T. Neyer, and S. S. Hanna, Bull. Am. Phys. Soc. **30**, 1284 (1985).
[33] A. E. Stuchbery, L. D. Wood, R. A. Bark, and H. H. Bolotin, Hyperfine Interact. **29**, 119 (1984).
[34] G. J. Lampard, H. H. Bolotin, C. E. Doran, L. D. Wood, I. Morrison, and A. E. Stuchbery, Nucl. Phys. A **496**, 589 (1989).
[35] K. Auerbach, K. Siepe, J. Wittkemp, and H. J. Korner, Phys. Lett. **23**, 367 (1966).
[36] G. Menzen, A. Wolf, H. Lawin, G. Lhersonneau, and K. Sistemich, Z. Phys. A: At. Nucl. **321**, 593 (1985).
[37] G. K. Hubler, H. W. Kugel, and D. E. Murnick, Phys. Rev. C **9**, 1954 (1974).
[38] H. Mach, *JYFL Annual Report* (University of Jyväskylä, Jyväskylä, 2003).
[39] A. Dewald *et al.*, Phys. Rev. C **78**, 051302 (2008).
[40] S. Frauendorf, Nucl. Phys. A **677**, 115 (2000).
[41] S. Nilsson and I. Ragnarsson, *Shapes and Shells in Nuclear Structure* (Cambridge University, Cambridge, 1995).
[42] A. E. Stuchbery, Nucl. Phys. A **589**, 222 (1995).
[43] M. Sambataro and A. E. L. Dieperink, Phys. Lett. B **107**, 249 (1981).
[44] O. Prior, F. Boehm, and S. G. Nilsson, Nucl. Phys. A **110**, 257 (1968).
[45] Y. S. Chen and S. Frauendorf, Nucl. Phys. A **393**, 135 (1983).
[46] G. Gürdal *et al.*, Phys. Rev. C **82**, 064301 (2010).